Journal of Sol-Gel Science and Technology (2025) 115:98–114
https://doi.org/10.1007/s10971-025-06783-9

ORIGINAL PAPER

# Multi-substituted barium hexaferrite with magnetoplumbite structure for microwave high-frequency applications

Ebtesam E. Ateia[1] · Yousra Yasser[1] · Amira S. Shafaay[1]

Received: 1 February 2025 / Accepted: 26 April 2025 / Published online: 21 May 2025


## Abstract

Barium hexaferrite (BHF) presents significant potential for different technological applications. By doping BHF with different substitution cations, a range of samples exhibiting diverse electrical and magnetic properties can be created. Gadolinium ($Gd^{3+}$) was used as an isovalent substitution for $Fe^{3+}$. On the other hand, Zirconium ($Zr^{4+}$), Zinc ($Zn^{2+}$) and Nickel ($Ni^{2+}$) were used as heterovalent substitutions for $Fe^{3+}$ as tetravalent and divalent elements. The structure, surface morphology characteristics and magnetic behavior of the samples were investigated. X-ray diffraction pattern (XRD), Field Emission Scanning Electron Microscope (FE-SEM), and Raman spectroscopy analysis (RSA) were used to evaluate the microstructure and establish the presence of the hexagonal phase as the main phase for the prepared samples. The average crystallite sizes obtained from XRD measurements ranged from 29 to 44 nm, while the grain sizes estimated through FE-SEM varied between 56 and 94 nm. X-Ray Photoelectron Spectroscopy (XPS) was used to determine quantitative elemental composition and the change in valencies due to substitution. The analysis used Vibrating Sample Magnetometry (VSM) to study the different magnetic properties of the samples. The composition $BaFe_{11.5}Gd_{0.5}O_{19}$ exhibited a minimum saturation magnetization of 38.753 emu/g, characterized by an average ionic radius of the B-sub-lattice measuring 0.938 Å, a minimum crystallite size of 29.577 nm, and a maximum coercivity value of 4639.5 Oe. While the composition $BaFe_{11.5}Zr_{0.5}O_{19}$ with a B-sub-lattice average ionic radius of 0.56 Å has the maximum saturation magnetization of 57.226 emu/g with the minimum coercivity of 2061 Oe. The high-frequency response of the BHFNPs demonstrates that they are capable of functioning in the frequency range of 8.5–13.17 GHz. The barium hexaferrite (BHF) powders synthesized in the present study exhibit high saturation magnetization, high coercivity, minimal magnetic loss, high chemical stability, and significant magnetic anisotropy, making them a strong candidate for high-frequency applications such as communication devices, and electromagnetic shielding.

## Graphical Abstract

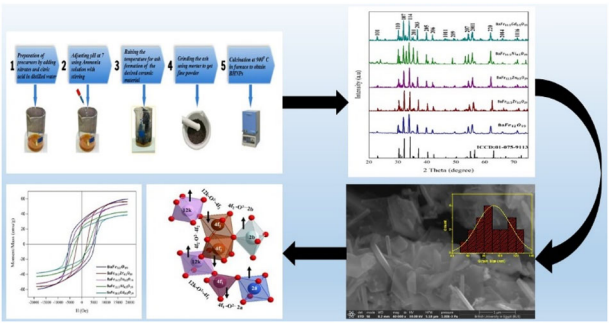

✉ Ebtesam E. Ateia
ebtesam@sci.cu.edu.eg

[1] Physics Department, Faculty of Science, Cairo University, Giza, Egypt

**Keywords** Magnetoplumbite structure · Magnetic parameters · Magnetic anisotropy · Lattice strain

**Highlights**

- The XRD analysis confirms that the samples prepared through the citrate auto-combustion method display an ideal hexagonal structure.
- The isovalent substitution provides a lower crystallite size than the heterovalent substitution.
- The barium hexaferrite (BHF) powders synthesized exhibit high saturation magnetization, high coercivity, minimal magnetic loss, high chemical stability, and significant magnetic anisotropy.
- The analysis of the binding energy (BE) reveals that both the undoped and doped BHFs exist as single-phase materials, free from any further contamination phases.
- The analysis reveals that the synthesized barium hexaferrite samples function at frequencies ranging from 8.5 to 13 GHz within the X band frequency spectrum, which is advantageous for the advancement of nano devices that operate in ultra-high frequency bands.

## 1 Introduction

Hexaferrite nanoparticles (*HFNPs*) have gained prominent status in several technological domains in recent years, attributed to their physical and chemical stability, elevated saturation magnetization, substantial coercivity, high Curie temperature, and minimal dielectric losses [1–4]. These materials find applications in a range of devices: including microwave electronics, biomedical applications, and permanent magnets, among others [5–8]. The scientific community has put enormous effort into the fabrication of high-efficiency microwave absorbing materials with properties such as high reflection loss, a large absorption bandwidth, and good thermal stability for applications like isolators, circulators, phase shifters, miniature antennas, and absorbers [9–13]. Hexaferrites are hard ferrites that are the best microwave materials in the 1–100 GHz band. They possess high coercivity and a natural resonance frequency in the gigahertz region with very low eddy loss [9, 14].

The *HFNPs* can be categorized into six distinct types, determined by their chemical composition. The M-type forms one of the most significant categories, Strontium (*Sr*), barium (*Ba*), lead (*Pb*), and calcium (*Ca*) ions can be substituted in the M site atoms, whereas cobalt (*Co*), nickel (*Ni*), and zinc (*Zn*) ions can be substituted in the B site atoms [15–18]. The crystal structure of BHF is composed of S (spinel) and R (hexagonal) blocks. The unit cell consists of the RSR*S* sequence illustrated in Fig. 1. The R* and S* blocks exhibit the same atomic arrangement as the R and S blocks, but they are rotated 180° along the c-axis. In this context, R is associated with $BaFe_6O_{11}$ while S is linked to $Fe_6O_8$. In the BHF crystal, five crystallographic sites are occupied by iron metal ions. Among these, the $4f_1$ tetrahedral sites (A sites) and *2a* octahedral sites (B sites) are located in the S block, while the $4f_2$ octahedral and *2b* trigonal bipyramidal sites are found in the R block. Additionally, the *12k* octahedral sites are situated at the *R–S* interface. External dopants, crystallite/grain size, sintering temperature, and synthesis method significantly affect the physical characteristics of M-type HFs [19–23].

Composites based on magnetic materials have garnered attention for their low conductivity and significant magnetic loss. Various approaches have been made to enhance the magnetic loss in magnetic materials, such as one-dimensional magnetic chains, core–shell structures, and controlled structural defects. The concept of changing the magnetic properties has received much attention from many researchers, one effective method for modifying M-type ferrites involves substituting $Fe^{3+}$ ions with various cations [24, 25]. The introduction of non-magnetic ions, such as zirconium ions ($Zr^{4+}$) and zinc ions ($Zn^{2+}$), has been investigated to achieve higher saturation magnetization values. These ions are likely to occupy the tetrahedral sites

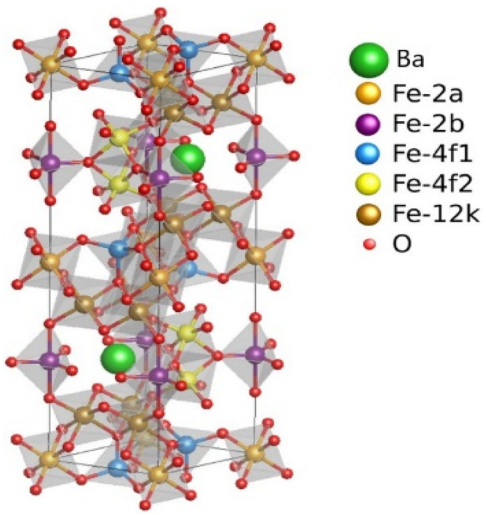


**Fig. 1** Schematic representation of hexagonal nanoparticles and the crystal structure of M-type $BaFe_{12}O_{19}$. The polyhedra in various colors illustrate the distinct $Fe^{3+}$ sites along with their surrounding $O^{2-}$ ions, highlighted in red. The green spheres represent the $Ba^{2+}$ ions

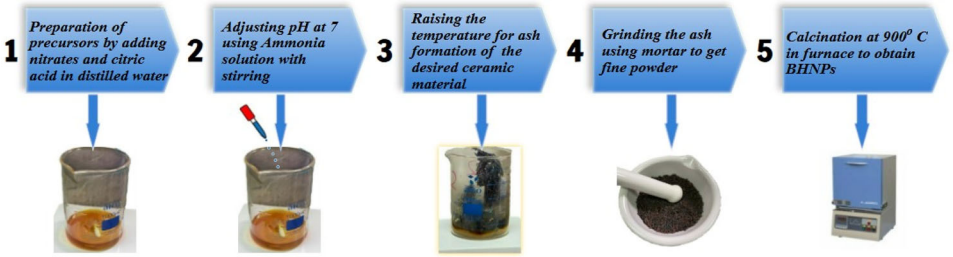


**Fig. 2** Chart for citrate auto combustion method

(*A site*), which are in opposition to the octahedral sites (*B site*) in M-type ferrites, thereby enhancing the overall magnetic moment [26]. On the other hand, substituting a magnetic cation at the B site will influence the overall magnetic moment due to the magnetic characteristics of the dopant cation. For instance, research has examined the impact of doping with $Ni^{2+}$, and it was found that this substitution leads to a reduction in both the net magnetization and the coercive field [27–29].

The spin coupling between the *4f* electrons of rare earth elements and the *3d* electrons of magnetic ions is pivotal in affecting the magnetic ordering of ferrites. Permanent ferromagnets have utilized this property, and interaction with a stable *f* electron can induce ferromagnetism in a nearly ferromagnetic itinerant electron system [30–32]. Rare earth $Gd^{3+}$ substitution has attracted much interest among researchers due to its unique ferromagnetism with a spin magnetic moment as significant as 7.9 $\mu_B$. Its effect on the structural, and dielectric properties of *BHF* has been studied. Typically, this substitution introduces more complex relaxation and conduction mechanisms due to the presence of additional heterovalent ions, which enhances the absorption and shielding characteristic of these materials [33–35].

The primary aim and novelty of this research are to prepare barium hexaferrite nanoparticles (*BHFNPs*) by substituting $Fe^{3+}$ ions with different divalent, trivalent and tetravalent cations to modify the magnetic parameters to levels that are appropriate for application in electronic circuits, aiming to reduce microwave frequency (*MWF*) and radio frequency interference (*RFI*). This will be carried out through the synthesis of $BaFe_{11.5}D_{0.5}O_{19}$; where $D = Zr^{4+}$, $Zn^{2+}$, $Ni^{2+}$ and $Gd^{3+}$ using the citrate auto-combustion technique.

## 2 Methodology

### 2.1 Materials used

All chemicals $Ba(NO_3)_3{\cdot}6H_2O$ (99%), $Zr(NO_3).6H_2O$ (98%), $Zn(NO_3)_2.6H_2O$ (99.9%), $Ni(NO_3).6H_2O$, $Gd(NO_3)_2.6H_2O$ (99%), $Fe(NO_3)_3{\cdot}6H_2O$ (98%), citric acid [$C_4H_8O_7$], and ammonia solution (33%) were obtained from (LOBA, India) Fig. 2.

### 2.2 Experimental technique

Numerous synthesis methodologies for fabricating metal oxide compounds have been developed, including solid-state, co-precipitation, auto-combustion, hydrothermal, and microemulsion techniques, etc. [23]. The synthesis of *BHF* samples was achieved through the citrate auto-combustion method, which is favored for its simplicity, cost-effectiveness, and capability to yield fine and homogeneous powders. Additionally, it controlled particle size, reduced agglomeration, and enhanced surface area and mesoporosity through rapid citrate-nitrate decomposition. $Zn^{2+}$, $Zr^{4+}$, $Ni^{2+}$ and $Gd^{3+}$ substituted, *BHF* was synthesized with a citric acid to metal nitrate ratio of 1:1. Citric acid is employed in this method as a chelating agent to create a homogeneous, stable, and transparent solution. The solution of ammonia was mixed drop wise using a burette to bring the *pH* of the solution to 7, which also improves the binding of cations to citrate and contributes to the stability and homogeneity of solutions [23, 36]. The resultant solution was heated at 80–200 °C with continuous magnetic stirring. A dark brownish gel was obtained with the evaporation of excess water. The precursor material was ground into a fine powder form with a mortar and pestle. During the sintering process (900 °C for 6 h heat rate 4 °C/min) as mentioned in previous literature [2, 3, 19].

### 2.3 Characterizations and measurements

X-ray diffraction (analytical-X'pertpro, Cu Kα1 radiation, λ = 1.5404 Å, 45 kV, 40 mA, Netherlands) was employed to identify phase formation and investigate the crystal structure. Raman Spectroscopy was used to analyze the composition of the structures and observe variations in vibrational frequency associated with chemical bonds. For morphological investigation, the Field Emission Scanning Electron Microscope (ThermoFisher (USA) Quattro S Field Emission Gun, Environmental *SEM*) was utilized. X-ray Photoelectron Spectroscopy (XPS) via K-ALPHA (Thermal

Fisher Scientific, USA), with monochromatic 400 µm spot X-ray Al K-alpha radiation using CASAXPS software at energies ranging from 0 to 1200 eV, was used to investigate the chemical states of different elements in the synthesized samples. The Vibrating Sample Magnetometer *(VSM)* was employed at room temperature to acquire the magnetic hysteresis loops (*M–H* loops) at a maximum field of 20 kOe, Lake Shore 7410.

## 3 Results and discussion

### 3.1 Structural analyses

#### 3.1.1 XRD analysis

Figure 3 presents *XRD* powder patterns of $BaFe_{11.5}D_{0.5}O_{19}$ ($D = Zr^{4+}$, $Gd^{3+}$, $Zn^{2+}$, $Ni^{2+}$) BHFs. The Full-Proof software is utilized in the XRD profile fitting process via the setup of the space group *P63/mmc (No. 194)*. The study facilitates the monitoring of changes in the crystalline structure of *BHF* relative to the doped elements. The ionic radii are systematically arranged from the narrowest to the widest. *XRD* analysis has demonstrated that all peaks align precisely with the standard theoretical pattern associated with pure *BHF*, indexed as (*ICCD 01-075-9113*). The diffraction pattern for *BHF* doped phases exhibits eleven broad peaks at 30.4°, 32.3°, 34.2°, 37.2°, 40.4°, 42.6°, 55.2°, 56.6°, and 63.2°, corresponding to the indices (*hkl*): (*110*), (*107*), (*114*), (*203*), (*205*), (*206*), (*217*), (*2011*), and (*220*) [1]. The lack of secondary phases validates the single crystal phase of $BaFe_{11.5}D_{0.5}O_{19}$, suggesting that the doped ions of $Zr^{4+}$, $Zn^{2+}$ and $Gd^{3+}$ have successfully filled the crystallographic sites of $Fe^{3+}$ ions.

The analyzed sample $BaFe_{11.5}Ni_{0.5}O_{19}$ reveals the presence of secondary phases and impurity peaks linked to $\propto$-$Fe_2O_3$. The refinement includes two phases: $BaFe_{11.5}$-$Ni_{0.5}O_{19}$ and $\propto$-$Fe_2O_3$. The phase composition indicates that $\propto$-$Fe_2O_3$ constitutes 26.87%, whereas $BaFe_{11.5}Ni_{0.5}O_{19}$ accounts for 73.13%. The detected secondary phases can affect magnetic properties by altering crystallographic orientation, introducing defects, or establishing interfacial magnetic interactions [1, 11, 37]. Nevertheless, in this instance, we are unable to clearly identify the impact due to several factors. The low concentration of $\propto$-$Fe_2O_3$ impurities, in comparison to the predominant phase, indicates that $\propto$-$Fe_2O_3$ (hematite) exhibits weak ferromagnetic or antiferromagnetic characteristics at room temperature [37].

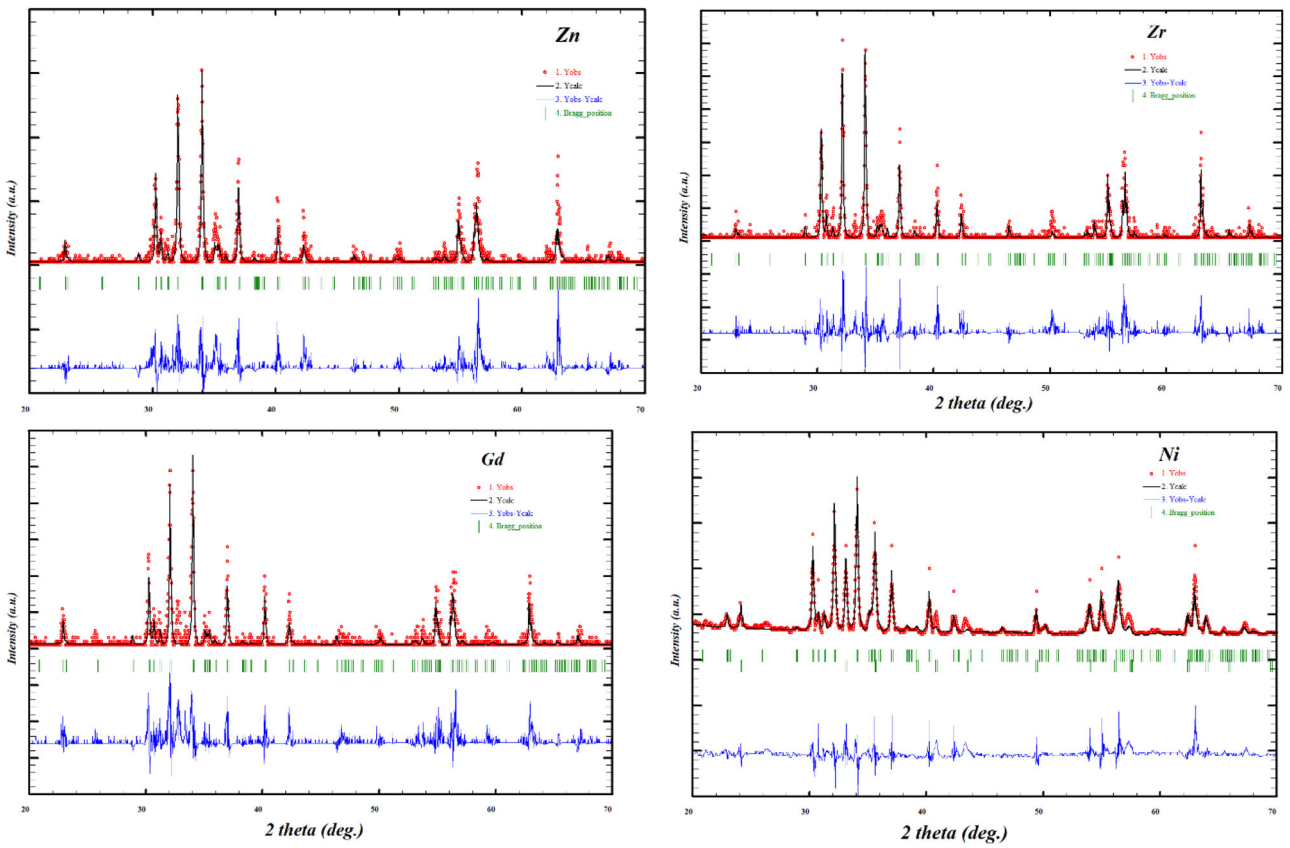


**Fig. 3** The XRD patterns of $BaFe_{11.5}D_{0.5}O_{19}$ ($D = Zr, Zn, Ni, Gd$) compared with *ICCD* card. The vertical sticks at the bottom show the calculated position for the peaks from $BaFe_{11.5}D_{0.5}O_{19}$

**Table 1** Lattice parameters (*a, c*), unit cell volume (*V*), molecular weight (*M*), X ray density ($\rho_X$), crystallite size (*D*) with both methods Scherrer and Williamson–Hall, ionic radii (*IR*) of Fe and the dopants, strain ($\varepsilon$), of the prepared samples

| Sample | IR (Å) | | a (Å) | c (Å) | c/a | V ($A^3$) | M (g/mol) | $\rho_X$ ($g/cm^3$) | D (nm) Sch. | D (nm) W-H | FWHM (114) | $\varepsilon*10^{-4}$ | Grain Size (nm) |
|---|---|---|---|---|---|---|---|---|---|---|---|---|---|
| BHF | *Tetra* | *Octa* | 5.890 | 23.195 | 3.938 | 696.876 | 1111 | 5.296 | 29.840 | 42.626 | 0.29 | 14 | 94.510 |
| | 0.490 | 0.645 | | | | | | | | | | | |
| Zr | *Tetra* | | 5.871 | 23.176 | 3.947 | 692.035 | 1245 | 5.973 | 44.060 | 38.139 | 0.19 | −9 | 91.970 |
| | 0.560 | | | | | | | | | | | | |
| Zn | *Tetra* | | 5.882 | 23.154 | 3.936 | 693.773 | 1116 | 5.343 | 40.930 | 36.232 | 0.21 | −12 | 64.940 |
| | 0.680 | | | | | | | | | | | | |
| Ni | *Octa* | | 5.899 | 23.249 | 3.941 | 700.700 | 1113 | 5.274 | 38.080 | 30.836 | 0.22 | −14 | 59.610 |
| | 0.690 | | | | | | | | | | | | |
| Gd | *Octa* | | 5.894 | 23.270 | 3.947 | 700.129 | 1162 | 5.512 | 36.040 | 29.577 | 0.24 | −19 | 56.810 |
| | 0.938 | | | | | | | | | | | | |

Additionally, the uniform distribution of ∝-$Fe_2O_3$ nanoparticles may result in a "dilute" magnetic system, where interfacial coupling effects are reduced, and the overall bulk properties remain largely unaffected.

The lattice parameter values (*a, c*) and the unit cell volume (*V*) are determined using the subsequent equations [19, 20]

$$\frac{1}{d^2} = \frac{4}{3}\left(\frac{h^2 + hk + k^2}{a^2}\right) + \frac{l^2}{c^2} \tag{1}$$

$$V = \sqrt{\frac{3}{4}}a^2 c \tag{2}$$

Where d is the distance between planes of atoms. The addition of cations with varying ionic radii into the BHF system changes slightly the lattice parameters (*a,c*), and consequently the volume of the cell as illustrated in Table 1.

This is attributed to the modification in the principle of occupation of the crystallographic spots by the doped elements, along with the alterations in both the charge and spin states of the $Fe^{3+}/Fe^{2+}$ iron cations [38].

Additionally, the c-axis, which is easily magnetized and perpendicular to the basal plane, exhibits a greater change compared to the lattice constant *a*, which experiences a slight change. The values of constant c undergo a notable alteration due to the anisotropic characteristics of hexagonal ferrites [38].

The ratio *c/a* as shown in the Table determines the degree of structural distortions. For the investigated samples the ideal *c/a* ratio being lower than 3.98 ratifies that all samples have an M-type HFs arrangement [15, 39].

This ratio is closely related to the magnetic properties of the prepared samples through structural and magneto crystalline anisotropy (K) effects as will be discussed later.

Furthermore, the crystallite size (D) of NPs is obtained using the following Scherer Equation [40–42],

$$D = \frac{k\lambda}{\beta \cos\theta} \tag{3}$$

Where β is the width of the diffraction line observed at its full half intensity, k is called the shape factor, which usually has a value of about 0.9, and λ is the X-ray source wavelength used in XRD.

The shift, broadening and intensity of XRD peaks are all related to the change of ionic radii of $Fe^{3+}$ (Tetra: 0.49 Å, Octa: 0.645 Å) with the dopants; $Zr^{2+}$ (Tetra: 0.56 Å), Zn (Tetra: 0.68 Å), $Ni^{2+}$ (Octa: 0.69 Å) and $Gd^{3+}$ (Octa: 0.938 Å). These changes in succession lead to changes in lattice parameters, volume and crystallite size affecting also grain size which is obtained from FE-SEM shown in the table [43].

Another analysis to determine the crystallite size ($D_{W\text{-}H}$) through the Williamson–Hall (W-H) equation, allows for the determination of strain (ε) for each sample [44, 45]. A plot between β Cosθ and 4Sinθ known as the W–H plot provides information on ε [46].

The sign of the slope indicates the nature of the strain, a positive slope corresponds to tensile strain whereas a negative slope corresponds to compressive strain. The values of induced strain can be calculated using Eq. (4) and tabulated in Table 1,

$$\beta \cos\theta = \frac{k\lambda}{D} + 4\varepsilon \sin\theta \tag{4}$$

The decrease in micro-strain can be explained by the stress field from grain boundaries causing deviations of atoms in the crystallites from their ideal positions. This effect is primarily concentrated in a region near the grain boundaries, which not only creates a local strain but also alters the lattice parameters. The local strain induced by the

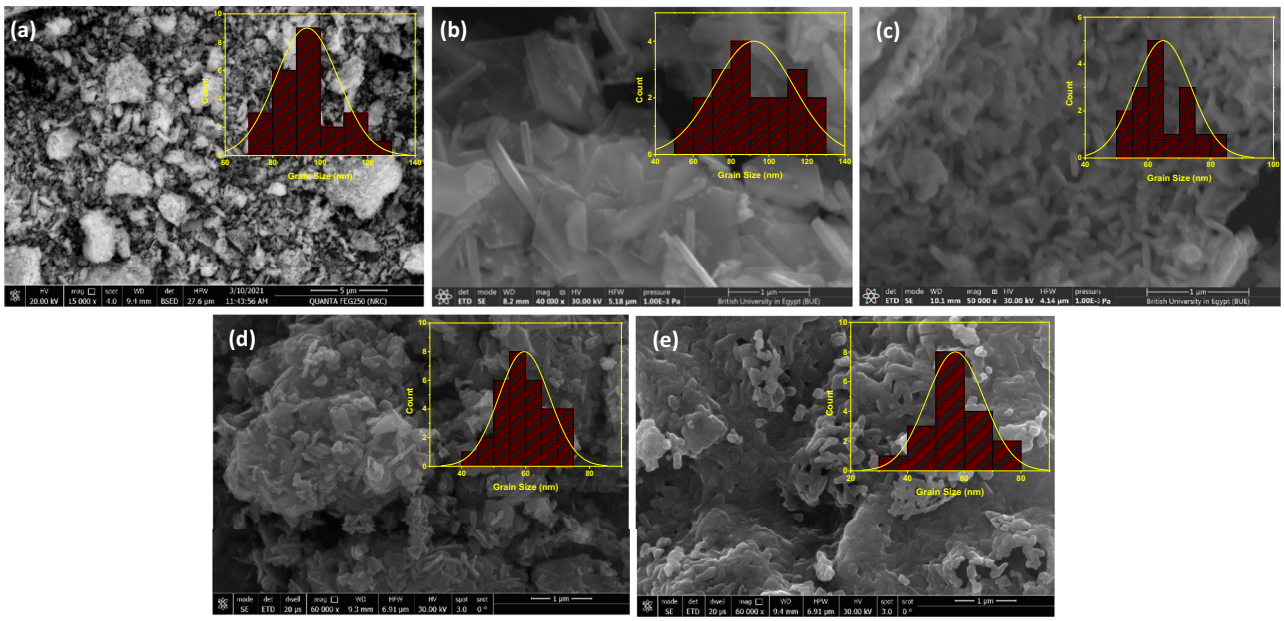


**Fig. 4** **a–e** FE-SEM of: **a** $BaFe_{12}O_{19}$, **b** $BaFe_{11.5}Zr_{0.5}O_{19}$, **c** $BaFe_{11.5}Zn_{0.5}O_{19}$, **d** $BaFe_{11.5}Ni_{0.5}O_{19}$, **e** $BaFe_{11.5}Gd_{0.5}O_{19}$

substitution of $Zr^{4+}$, $Zn^{2+}$, $Ni^{2+}$, and $Gd^{3+}$ may be responsible for the decrease in $D_{W\text{-}H}$.

The X ray density ($\rho_x$) mainly varies with the molecular mass ($M$) for each sample with respect to the molar mass of the dopants, $Zr^{4+}$ = 322.25 amu, $Zn^{2+}$ = 65.38 amu, $Ni^{2+}$ = 58.69 amu and $Gd^{3+}$ = 157.25 amu, by following relation [40, 47, 48],

$$\rho_x = \frac{Z\,M}{N_A\,V} \tag{5}$$

where $Z = 2$ is the appropriate number of molecules per unit cell and $N_A$ is Avogadro's number. All the mentioned data are tabulated in Table 1, which closely matches the values reported in the literature [39, 47].

### 3.1.2 FE-SEM analysis

The magneto-plumbite arrangement is clearly seen in the flat hexagonal areas of the particles, as illustrated in the corresponding enlargement images in Fig. 4a–e. FESEM images indicate that the specimens consisted of aggregated grains forming clusters of various sizes and shapes. The distribution of particles is uniform but their sizes are vary throughout the sample [49]. The existence of the well-defined hexagonal grains indicates a notable level of crystallinity and structural uniformity throughout the crystal lattice. The microphotography illustrates the dense arrangement of the particles and their uniform distribution, indicating that BHF grains exhibited a platelet-like morphological shape characterized by a planar nature and hexagonal-shape [21, 50]. The grain size distribution was analyzed using ImageJ software, and tabulated in Table 1. The calculated data is consistent with the trend of crystallite size values calculated from *XRD*.

Nanomaterials are observed to slightly agglomerate in hexa-shapes for $Zn^{2+}$ and $Gd^{3+}$ than in $Zr^{4+}$ and $Ni^{2+}$ substituted samples, showing poly-disperse arrangements. This can be explained by the change in ionic radii for each element at their preferred occupation sites. It is known from the survey that $Zr^{4+}$ and $Zn^{2+}$ prefer the A (Tetrahedral) sites, unlike *Ni* and *Gd* which prefer the B (Octahedral) sites. This will be confirmed by Raman spectroscopy analysis in Fig. 5 [51, 52].

### 3.1.3 Raman spectroscopy analysis (RSA)

*RSA* can be used to determine the microstructure of materials and the change in vibrational frequency for chemical bonds [53]. The *RSA* of the parent and substituted BHF has been determined at 300 *K* within the range of 200–800 $cm^{-1}$ as seen in Fig. 5a–d. To identify the positions of the vibration modes, the RS is fitted with mathematical functions (Lorentzian functions). The observed peaks represent distinct vibrational modes as proposed by group theory, indicating the existence of 42 Raman-active vibrational modes ($11A_{1g} + 14E_{1g} + 17E_{2g}$) within the M-type HFs structure [51]. The peaks at 407, 506, 600, 675, and 740 $cm^{-1}$ of $A_{1g}$ symmetry correspond to the *12k, 12k + 2a* (mixed band), $4f_2$, *2b*, and $4f_1$ sites, respectively. The peak at 320 $cm^{-1}$ of $E_{2g}$ symmetry is linked to the *12k* site, and the 2b site exhibits significant oscillation; any alteration in this site effectively disrupts the crystal symmetry owing to its proximity to the Ba site [2, 51].

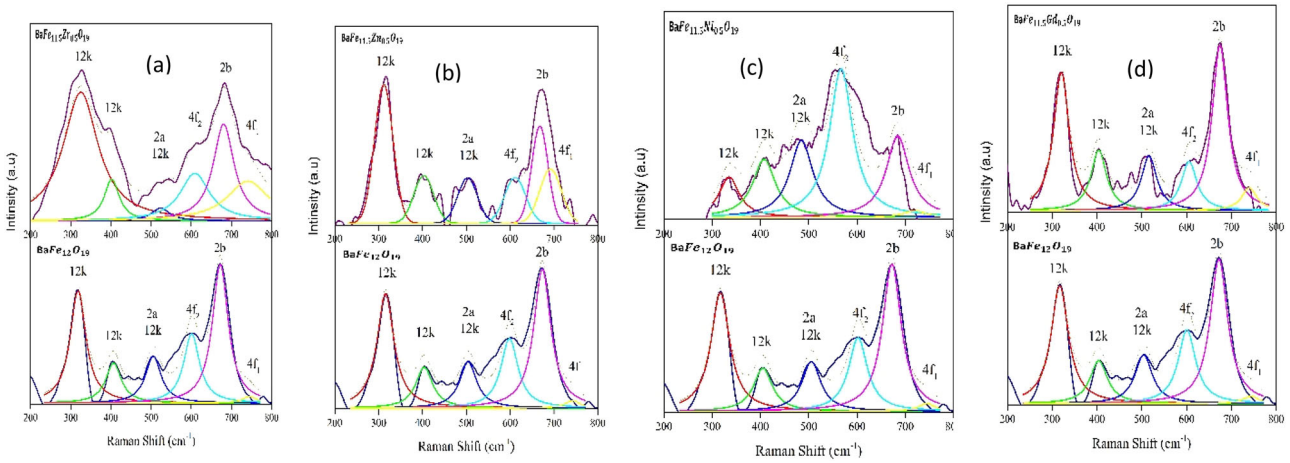


**Fig. 5** **a–d** RSA of: **a** $BaFe_{11.5}Zr_{0.5}O_{19}$, **b** $BaFe_{11.5}Zn_{0.5}O_{19}$, **c** $BaFe_{11.5}Ni_{0.5}O_{19}$, **d** $BaFe_{11.5}Gd_{0.5}O_{19}$

It is clear from the figure that, the vibration bands (VB) in the substituted $BaFe_{11.5}D_{0.5}O_{19}$, where $D = Zr^{4+}$, $Zn^{2+}$, $Ni^{2+}$ and $Gd^{3+}$ are shifted compared to pure $BaFe_{12}O_{19}$. Accordingly, the vibration energy was changed, confirming that the dopants are incorporated into the BHF lattice. The occupation of D cations alongside the Fe sites can significantly influence the bonding strength between the surrounded oxygen atoms and the adjacent $FeO_6$ octahedron. From the survey, the $Zr^{4+}$ and $Zn^{2+}$ ions preferred the tetrahedral site corresponding to the $4f_1$ spin down site while $Ni^{2+}$ and $Gd^{3+}$ ions preferred the octahedral sites corresponding to the *12k, 2a* spin up and $4f_2$ spin down sites, depending on the electronic configuration of each element [29].

For $Zr^{4+}$ and $Zn^{2+}$ ions, the $4f_1$ peak shifted to a small Raman shift relative to the parent confirmed by the survey data. There is a slight shift at the *12k* peaks indicating that some of the cations may occupy the octahedral site. On the other hand, $Ni^{2+}$ and $Gd^{3+}$ ions show a shift at the octahedral sites, $Ni^{2+}$ shows shifting at spin up and spin down octahedral (*12k, 2a,* $4f_2$) sites. Additionally, the intensity of its peaks decreases and becomes broader suggesting increasing distortion of the $BaFe_{11.5}Ni_{0.5}O_{19}$ [51]. $Gd^{3+}$ mainly shows a shift at the spin down $4f_2$ site and a slight shift at the spin down $4f_1$ site, which may be the reason for its small magnetic saturation despite having the largest magnetic moment. Ultimately, the variation in the radius of ions among $Fe^{3+}$, $Zr^{4+}$, $Zn^{2+}$, $Ni^{2+}$, and $Gd^{3+}$ ions in B coordination leads to localized deformation and a shifting of vibrational bands within the deformed polyhedron [29].

### 3.1.4 XPS spectroscopy

The XPS innovation provides insights into the chemical state and composition of the substances present in the nanomaterials. The analysis of the binding energy (BE) reveals that both the undoped and doped BHFs exist as single-phase materials, free from any further contamination phases [54]. The survey scan spectra in Fig. 6 exhibit peaks corresponding to *Ba 3d*, *Fe 2p*, *Zr 3d, Zn 2p*, *Ni 2p*, *Gd 4d* and *O 1s* in the material. The *C 1s* peak at 284.5 eV is caused by contaminating carbon [54].

As shown in Fig.7, the BE values for $Ba^{2+}$ exhibit a spin–orbit doublet structure, corresponding to the $3d_{5/2}$ and $3d_{3/2}$ states of $Ba^{2+}$ at 779.65 and 794.79 eV, respectively, confirming the presence of $Ba^{2+}$ [54]. In the case of pure BHF, the *Ba* peak of the $3d_{5/2}$ core level is fitted by a single profile centered at 779.65 eV. In the doped samples the peaks of the $3d_{5/2}$ and $3d_{3/2}$ states are broader and deconvoluted into two components centered at 779.22 eV, 780.25 eV and 794.23 eV, 795.21 eV, respectively. The components with binding energies of 780.25 eV and 795.21 eV correspond to $Ba^{2+}$ ions, while the other components originate from the defects formed in the crystal lattice upon doping. These defects can induce drastic changes in *Ba–O* bonds resulting in a new component centered at 779.22 eV and 794.23 eV.

The refined XPS spectra of *Zr 3d* within $BaFe_{11.5}Zr_{0.5}O_{19}$ HF are presented in Fig. 8a. The *Zr* $3d_{5/2}$ and *Zr* $3d_{3/2}$ peaks for *Zr* ions are detected at a binding energy of 181.46 eV and 183.86 eV, respectively. This observation indicates a 4+ valence state for the *Zr* cation [55].

On the other hand, Fig. 8b shows that *Zn* $2p_{3/2}$ and *Zn* $2p_{1/2}$ are at BE 1021.06 eV and 1044.15 eV, respectively [47]. Finally, Fig. 8c, d for $Ni^{2+}$ and $Gd^{3+}$ ions show the *Ni* $2p_{3/2}$ and *Ni* $2p_{1/2}$ peaks to be within 854.53 eV and 872.17 eV and the peaks of *Gd 4d* appear in the range of 138.85 eV to 154.35 eV [33, 56].

Furthermore, Fig. 9 illustrates the peak of O 1s for BHFs. The peak that occurs at a binding energy of 528.25 eV relates to oxygen within the lattice, whereas the peak at 530.41 eV is linked to the existence of non-lattice oxygen [57]. Between 526 and 535 eV, multiple

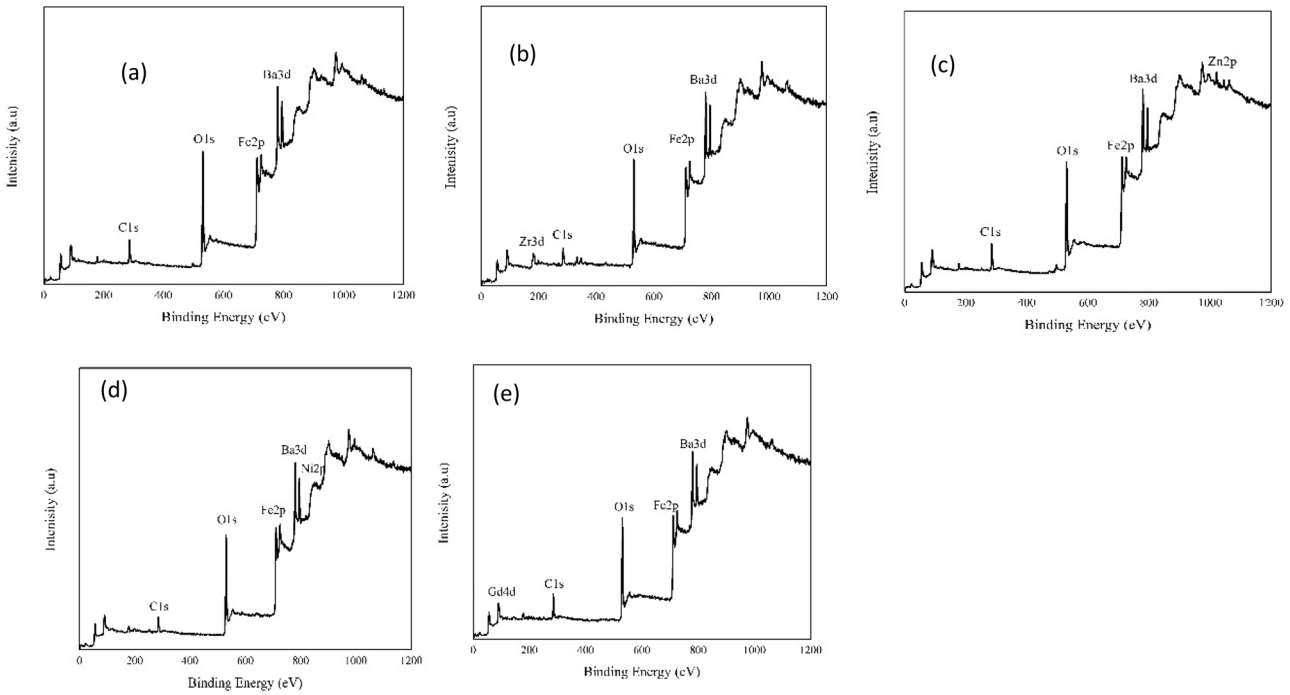


**Fig. 6** **a**–**e** XPS Servey graphs: **a** $BaFe_{12}O_{19}$, **b** $BaFe_{11.5}Zr_{0.5}O_{19}$, **c** $BaFe_{11.5}Zn_{0.5}O_{19}$, **d** $BaFe_{11.5}Ni_{0.5}O_{19}$, **e** $BaFe_{11.5}Gd_{0.5}O_{19}$

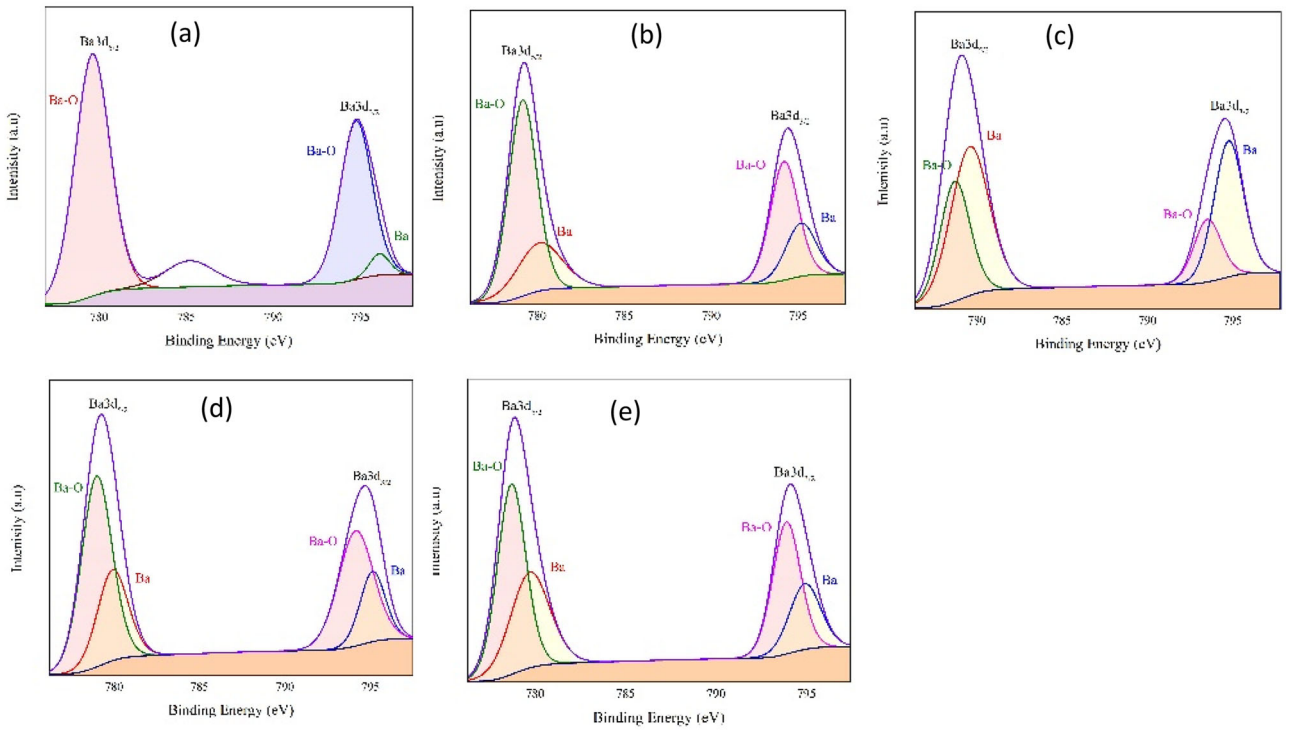


**Fig. 7** **a**–**e** XPS of Ba graphs: **a** $BaFe_{12}O_{19}$, **b** $BaFe_{11.5}Zr_{0.5}O_{19}$, **c** $BaFe_{11.5}Zn_{0.5}O_{19}$, **d** $BaFe_{11.5}Ni_{0.5}O_{19}$, **e** $BaFe_{11.5}Gd_{0.5}O_{19}$

signals are observed for oxygen 1s electrons. The oxygen signal at 529.08 eV is associated with ferrite, while the signal at 531.38 eV indicates the presence of oxygen defects [58].

These defects may be influenced by heating conditions and lattice distortion caused by dopants. The existence of oxygen defects can potentially increase the number of oxygen vacancies, thereby affecting magnetic properties

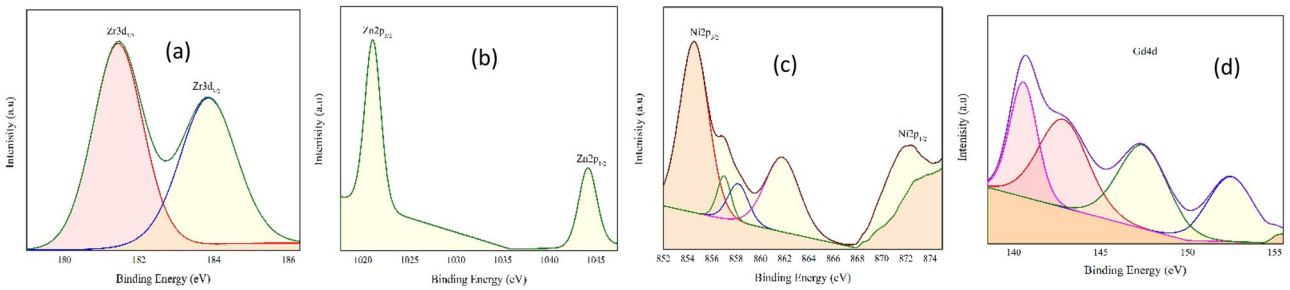


**Fig. 8** **a–d** XPS graphs: **a** Zr in $BaFe_{11.5}Zr_{0.5}O_{19}$, **b** Zn in $BaFe_{11.5}Zn_{0.5}O_{19}$, **c** Ni in $BaFe_{11.5}Ni_{0.5}O_{19}$, **d** Gd in $BaFe_{11.5}Gd_{0.5}O_{19}$

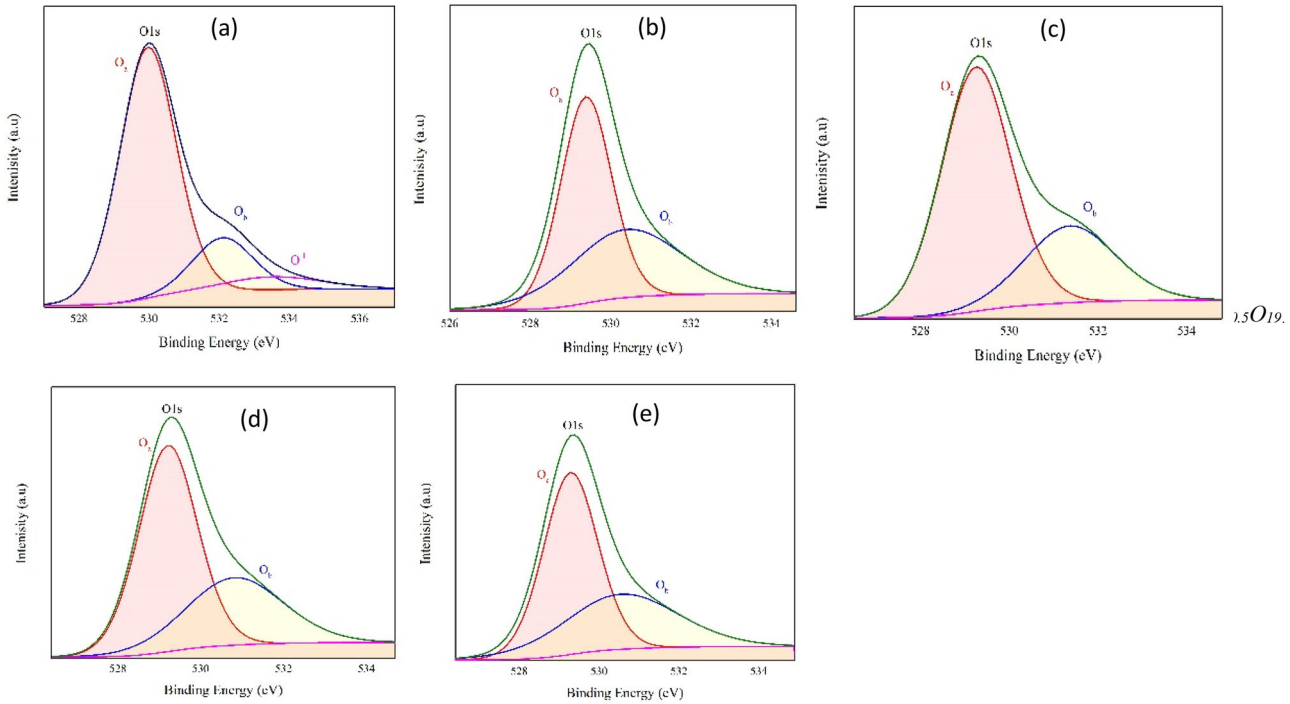


**Fig. 9** **a–e** XPS of Oxygen graphs: **a** $BaFe_{12}O_{19}$, **b** $BaFe_{11.5}Zr_{0.5}O_{19}$, **c** $BaFe_{11.5}Zn_{0.5}O_{19}$, **d** $BaFe_{11.5}Ni_{0.5}O_{19}$, **e** $BaFe_{11.5}Gd_{0.5}O_{19}$

[59]. This information is presented in Table 2, which displays the atomic percentage of $O_b$, representing the percentage of oxygen vacancies in each sample.

Figure 10 illustrates the two primary peaks at approximately 710 and 724 eV, corresponding to Fe $2p_{3/2}$ and Fe $2p_{1/2}$ across the prepared samples, respectively. The peaks can be distinguished into multiple peaks at energies of 710, 712, 715, 718, 723, 726, 730 and 733 eV. The peaks observed at 710 and 723 eV indicate $Fe^{2+}$ ions, while those at around 712 and 726 eV are linked to $Fe^{3+}$ ions. The remaining peaks are classified as satellite peaks [58].

The results indicate the presence of $Fe^{2+}$ ions in BHFs. The existence of $Fe^{2+}$ ions suggests that charge exchange occurs among $Fe^{2+}/Fe^{3+}$ and the dopant's ions. This alteration in valence state facilitates the incorporation of the ions into the lattice [58]. It can be concluded that in all established crystals, significant charge balancing occurs through the reduction of $Fe^{3+}$ to $Fe^{2+}$ which influences the magnetic behavior of the samples.

## 3.2 Magnetic measurements

### 3.2.1 Hysteresis loop

The hysteresis loops depicted in Fig. 11a illustrate the magnetic behavior of pure BHF with $BaFe_{11.5}D_{0.5}O_{19}$ ($D = Zr, Zn, Ni, Gd$) HFs. Both the undoped and doped samples exhibit hard ferromagnetic characteristics at room temperature. The changes in magnetic properties are mainly attributed to the *Fe* ions occupying various crystallographic positions and their exchange interactions [57].

The investigation revealed that the $Fe^{3+}$ ions within the $BaFe_{12}O_{19}$ phase are located at *12k*, *2a*, and *2b* spin up positions, as well as $4f_1$ and $4f_2$ spin-down positions. Due to

the conflicting magnetic moments of $Fe^{3+}$ ions at spin-up and spin-down locations, the overall magnetic moment is changed [60]. The theoretically estimated total magnetic moment per unit formula of BHFs ($n_{B,theo}$) is obtained via Eq. (6), in which (↑) and (↓) represent the magnetic moments of sublattices with spin-up and spin-down, respectively. For high-spin $Fe^{3+}$, and $Fe^{2+}$ the magnetic moments are approximately 5 $\mu_B$, and 4 $\mu_B$, respectively. While for $Zn^{2+}$, $Zr^{4+}$, $Ni^{2+}$, and $Gd^{3+}$, the magnetic moments are approximately, 0.0, 0.0, 2.8 $\mu_B$, and 7.93 $\mu_B$, respectively [2],

$$n_{B\,theo} = (2a)^{\uparrow} + (2b)^{\uparrow} + (12k)^{\uparrow} + (4f_1)^{\downarrow} + (4f_2)^{\downarrow} \quad (6)$$

**Table 2** The ratio of atomic % of $Fe^{3+}$ to atomic % of $Fe^{2+}$ and atomic % of Oxygen vacancies $O_b$ for BHF and $BaFe_{11.5}D_{0.5}O_{19}$ ($D$ = *Zr, Zn, Ni, Gd*)

| Sample | $Fe^{3+}/Fe^{2+}$ | $O_b$% |
|---|---|---|
| BHF | 1.928 | 17.260 |
| Zr | 1.974 | 41.930 |
| Zn | 1.560 | 29.000 |
| Ni | 1.449 | 38.830 |
| Gd | 0.953 | 35.260 |

The formula for the experimental magnetic moment ($n_{B,exp}$) is also calculated with Eq. (7), and its results are presented in Table 3 [61],

$$n_{\mathrm{B,exp}} = \frac{Molecular\ weight(M_W) \times Saturation\ magnetization(M_s)}{5585} \quad (7)$$

Based on the previous discussion it can be indicated that the magnetic moments ($n_B$) are predominantly contributed by *Fe* atoms, which are associated with half-*d* band filling. It has been determined that the introduction of *Zr, Zn, Ni, Gd*, and *Zn* as substitutes can result in either a reduction or an enhancement in the total magnetization of the system being examined compared to the pure BHF, contingent upon the particular crystallographic site occupied by the doped ions.

In the present study, all total theoretical magnetization values are higher than the experimental value. This difference, may be due to the random incorporation of $Zr^{4+}$, $Zn^{2+}$,$Ni^{2+}$ and $Gd^{3+}$ ions in possible sites, as well as the presence of different types of structural defects [62].

The remanent magnetization ($M_r$), coercivity ($H_c$), saturation magnetization ($M_s$), magneto crystalline anisotropy constant ($K$) and squareness ratio ($SR$) of the samples were obtained from magnetic hysteresis loops and tabulated

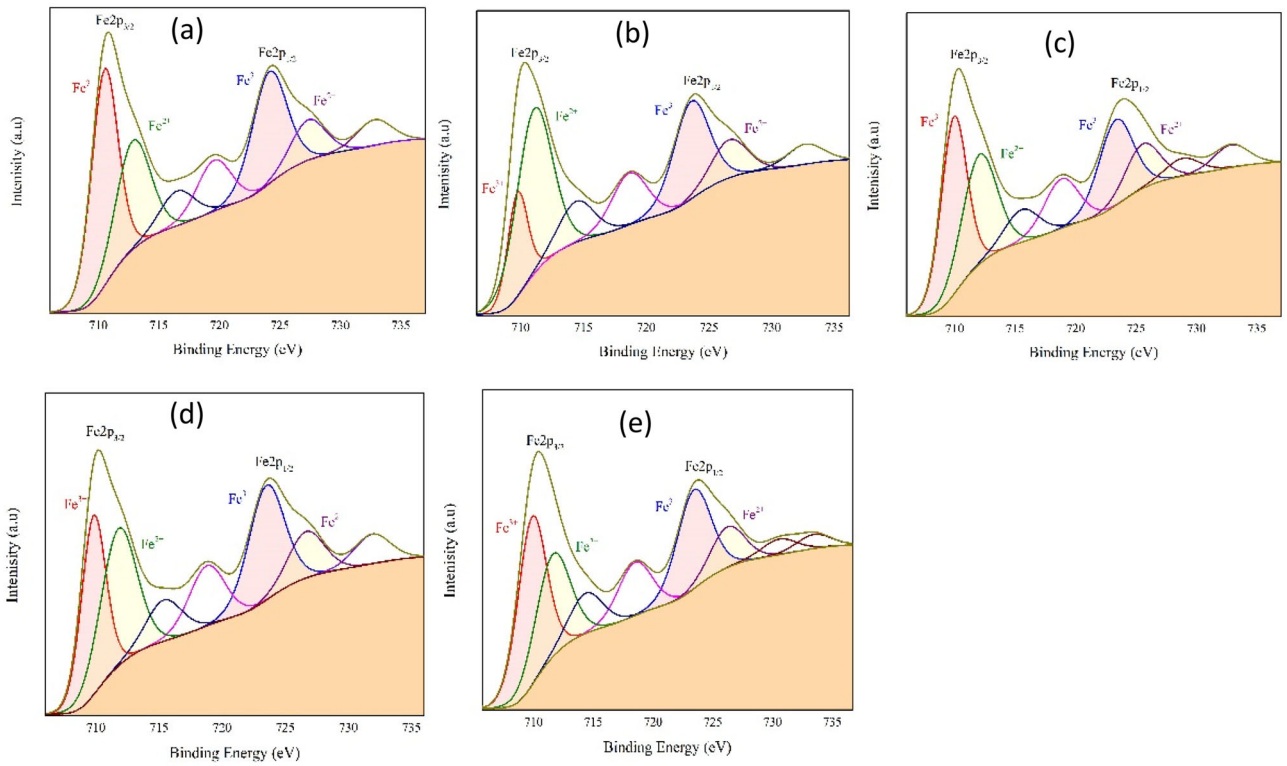


**Fig. 10** **a–e** XPS of Fe graphs: **a** $BaFe_{12}O_{19}$, **b** $BaFe_{11.5}Zr_{0.5}O_{19}$, **c** $BaFe_{11.5}Zn_{0.5}O_{19}$, **d** $BaFe_{11.5}Ni_{0.5}O_{19}$, **e** $BaFe_{11.5}Gd_{0.5}O_{19}$

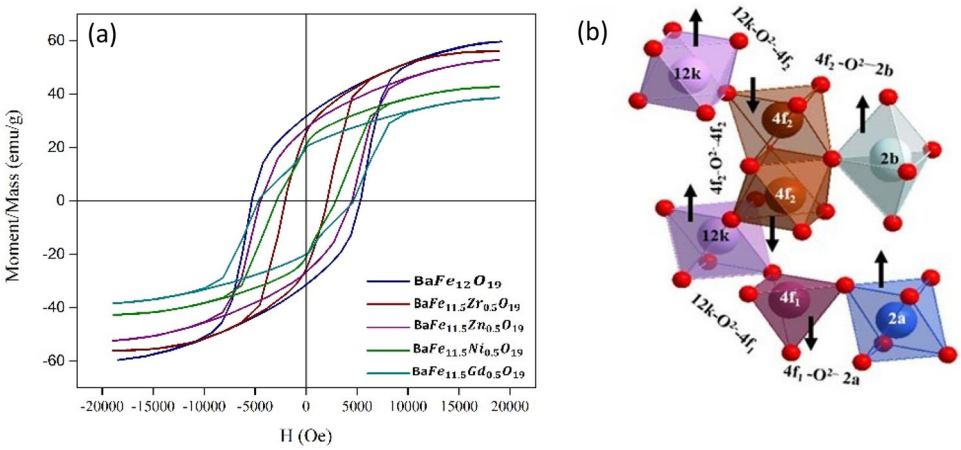


**Fig. 11** **a** VSM hysteresis loops of the samples. **b** Digram shows the destortion of the sites inside the lattice

**Table 3** Saturation magnetization ($M_s$) experimentally and LAS, remanent magnetization ($M_r$), coercivity ($H_c$), squareness ratio ($SR$), experimental magnetic moment ($n_{exp}$), SFD and microwave frequencies of the prepared samples compared to previous work

| Sample | $M_s$ (emu $g^{-1}$) | $M_s$ ($emug^{-1}$) LAS | $M_r$ ($emu.g^{-1}$) | $H_c$ (Oe) | $K_1*10^5$ ($erg/cm^3$) | SR | $n_{exp.}$ | SFD | $\omega_m$ (GHz) |
|---|---|---|---|---|---|---|---|---|---|
| BHF the present study | 59.636 | 61.152 | 31.556 | 5318 | 8.190 | 0.529 | 11.867 | 0.603 | 13.171 |
| Zr the present study | 56.077 | 57.226 | 25.525 | 2061 | 6.059 | 0.455 | 12.497 | 2.305 | 12.638 |
| Zn the present study | 52.536 | 54.993 | 27.166 | 4474 | 7.971 | 0.517 | 10.499 | 1.131 | 11.741 |
| Ni the present study | 42.68 | 43.191 | 21.061 | 2909 | 4.663 | 0.493 | 8.504 | 2.440 | 9.538 |
| Gd the present study | 38.615 | 38.753 | 19.833 | 4639 | 4.560 | 0.513 | 8.035 | 1.875 | 8.558 |
| $Ba_{0.5}Gd_{0.5}Fe_{12}O_{19}$ [33] | 29.480 | – | 17.770 | 1919 | 5.432 | 0.600 | – | – | 12.400 |
| $BaFe_{11}Al_1O_{19}$ [78] | 21.732 | – | 12.685 | 4847 | – | 0.583 | 4.212 | – | – |
| $Ca(ZrCo)_{0.8}Fe_{10.4}O_{19}$ [64] | 30.070 | – | 12.220 | 990 | – | 0.406 | 5.63 | – | – |

in Table 3. The substitution of non-magnetic ions $Zn^{2+}$ *and* $Zr^{4+}$ in $BaFe_{11.5}D_{0.5}O_{19}$ is anticipated to occupy most of the available spin-down sites $4f_1$ [27, 63–65]. Consequently, it reduces the number of $Fe^{3+}$ ions with a spin down orientation, leading to an increase in the magnetic moment density ($M_S$) compared to other dopants as demonstrated in the Table. The nonmagnetic dopants, such as $Zn^{2+}$ *and* $Zr^{4+}$ with no magnetic moment, may also decrease the super-exchange interaction within tetrahedral and octahedral sites ($4f_1$–*12a and* $4f_1$–*12k*). This behavior was previously documented in other diamagnetic substituted ferrites [66, 67]. Based on the fluctuations in Ms value and Raman spectroscopy data, it can be inferred that $Zr^{4+}$ and $Zn^{2+}$ ions substitute $Fe^{3+}$ ($5\mu_B$) ions in the aligned $4f_1$/*12k* sites. While $Ni^{2+}$ (2.83 $\mu_B$) ions occupy the anti-parallel octahedral *12k* site, partially compensating for the loss of $Fe^{3+}$ from this site.

The sample substituted with *Gd* shows a kink behavior, which occurs due to the varying magnetic responses exhibited by the hard and soft phases when subjected to an external magnetic field [68]. Additionally, the replacement of $Fe^{3+}$ ions with $Gd^{3+}$ ions leads to decreased magnetization values, despite Gd having a higher magnetic moment value (7.94 μB) compared to Fe (5 μB). The positioning of *Gd* at spin up (*2a, 12k*) with magnetic moment along *c* positive (as shown in Fig. 11b rather than spin down ($4f_2$) can contribute to the reduction in the total magnetic moment in BHF [69]. Finally, there is an overall reduction in magnetization for the *[Fe-2a-↑][Gd-2a-↓]* and *[Fe-12k-↑][Gd-12k-↓]* configurations. The same behavior is reported for $Tb^{3+}$ ions ($n_B$=9.5 $\mu_B$) when doped into $Ba_{0.8}In_{0.2}Fe_{12-x}Tb_xO_{19}$ [70]. Hence, these results demonstrate that the magnetization of doped ferrite cannot be elucidated solely based on the magnetic moment of the doped ions.

The squareness ratio ($SR = M_r/M_s$) of the doped BHFs is approximately 0.5, indicating the presence of magnetostatic interaction. A higher SR is preferred for permanent magnets because it limits demagnetization and the dynamics of domain walls facilitated by coherent spin rotation, thereby increasing the coercivity [57]. The coercivity field ($H_c$) of each sample is calculated based on the (M-H) loops of all synthesized HFNPs shown in Fig. 11a. It is well established that the coercivity (*Hc*) of substituted barium hexaferrites (BHFs) is affected by factors such as shape anisotropy, magnetocrystalline anisotropy, and grain size, particularly in the case of noninteracting single-domain nanoparticles [24, 33, 71]. Furthermore, various other factors, including particle sizes and the existence of vacancies, also play a significant role. These factors primarily account for the observed coercivity value of ≈ 5318 G in the parent $BaFe_{12}O_{19}$ samples.

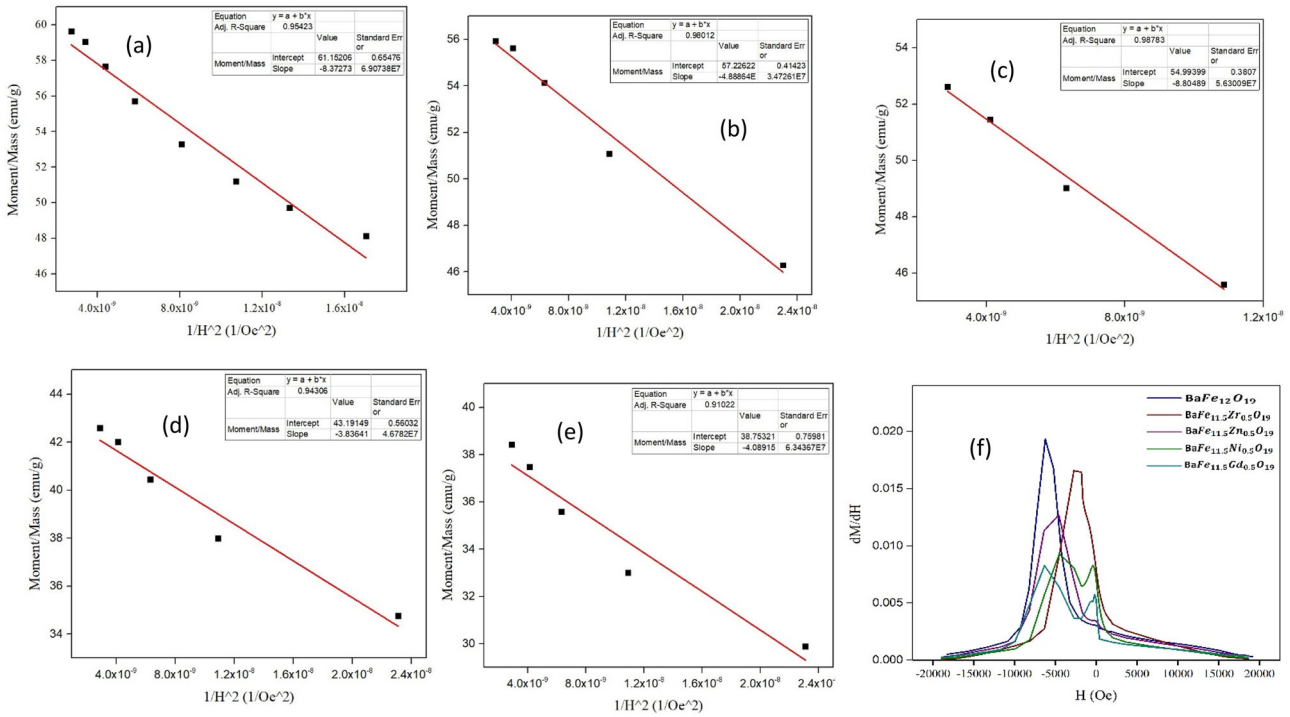


**Fig. 12** **a–f** The Fitting Plots of: **a** $BaFe_{12}O_{19}$, **b** $BaFe_{11.5}Zr_{0.5}O_{19}$, **c** $BaFe_{11.5}Zn_{0.5}O_{19}$, **d** $BaFe_{11.5}Ni_{0.5}O_{19}$, **e** $BaFe_{11.5}Gd_{0.5}O_{19}$, **f** Switching Field Distribution plot of the samples

The lowest *Hc* values are achieved for $Zr^{4+}$ and $Ni^{2+}$ doped BHFs. This reduction can be clarified by the changes in magnetocrystalline anisotropy *(K)* of the samples. It has been previously established that a single $Fe^{3+}$ ion on *2b* and $4f_2$ sites is the primary cause of uniaxial magneto-crystalline anisotropy of HFs [66].

Conversely, the highest coercivity for doped samples is achieved with $BaFe_{11.5}Gd_{0.5}O_{19}$. However, the ionic radius of $Gd^{3+}$ (≈0.938 Å) is considerably larger than that of $Fe^{3+}$ (≈0.645 Å). This size mismatch introduces lattice distortions, which in turn increases local strain. Such strain alters the crystal field environment around neighboring $Fe^{3+}$ ions, thereby enhancing the overall magnetic anisotropy as shown in Table 3. [62, 72, 73]. Moreover, this lattice strain may induce defects or stress fields that serve as pinning sites for domain walls, contributing to an increase in coercivity.

The relationship between coercivity and grain size can be described through the statements "coercivity increases with grain size" and "coercivity decreases with grain size," both of which can be valid under certain conditions. While these two statements may seem contradictory, they can coexist as accurate under specific conditions. In the present study, the magnetization processes occurring in a multi-domain sample lead to a reduction in both grain size and coercivity. However, this trend does not hold true for all samples examined, as variations in the types of cations encompassing both magnetic and non-magnetic cations, as well as differences in ionic radii and orbital configurations such as *3d* and *4f* contribute to differing behaviors.

### 3.2.2 Law of approach to saturation (LAS)

The saturation magnetization ($M_s$) is determined from Fig. 12 using the "Law of Approach to Saturation (LAS)" [21]. *LAS* is utilized to examine the magnetic data in the saturation region detailing the relationship between magnetization and the applied magnetic field $H \gg H_c$ [21],

$$M = M_s\left(1 - \frac{a}{H} - \frac{b}{H^2}\right) + \chi H \tag{8}$$

where $a$ is considered as a constant that depends on material properties, $H$ is an applied field, $b$ is the anisotropy parameter, and $\chi H$ represents the high-field differential susceptibility associated with the domains' spontaneous magnetization, which is relevant to the high-temperature examination. Thus, it is ignored for hysteresis loops at room temperature. Additionally, $a/H$ does not yield meaningful values. Consequently, Eq. (8) is modified as [21],

$$M = M_s\left(1 - \frac{b}{H^2}\right) \tag{9}$$

The experimental $M$ versus $1/H^2$ plot for the BHF and doped samples is illustrated in Fig. 12. Each sample produces a linear representation, suggesting that both the $a/H$ and $\chi H$ terms exert minimal influence. The slopes of the straight lines are used to determine the anisotropy parameter, while the intercept determined the Ms. The magnetocrystalline anisotropy constant ($K$), can be determines using the following equation [68, 74],

$$b = \frac{8\,K_1^2}{105\,M_s^2} \tag{10}$$

The data obtained are presented in Table 3.

In M-type hexaferrites, lower c/a ratios correspond to their specific structure, influencing how ions occupy lattice sites, which affects the alignment of magnetic moments [71]. Substitutions that alter the $c/a$ ratio can change the balance between spin-up and spin-down sites, thus affecting magnetic parameters. A higher $c/a$ ratio enhances uniaxial anisotropy, favoring high coercivity ($H_c$), $Gd^{3+}$ and $Ni^{2+}$ substituted HFs with $c/a$ ratios of approximately 3.941, and 3.947, respectively, demonstrate strengthened uniaxial magnetocrystalline anisotropy, leading to increased coercivity ($H_c$). $Gd^{3+}$ substituted $BaFe_{12}O_{19}$ with a $c/a$ ratio of around 3.947 exhibits $H_c$ values suitable for longitudinal recording media.

#### 3.2.3 Switching field distribution (SFD)

The $BaFe_{12}O_{19}$ and $BaFe_{11.5}D_{0.5}O_{19}$ ($D = Zr,\ Zn,\ Ni,\ Gd$) samples, exhibit a uniform magnetic behavior as a single phase, displaying smooth hysteresis loops. This finding can be verified through the analysis of the SFD, as illustrated by plotting the $dM/dH$ vs H curve in Fig. 12f. Magnetic susceptibility $\chi = dM/dH$ is employed to calculate the magnetic interaction present in different materials. The value of $\chi$ is linked to the switching or inversion field distribution (SFD).

The peak in $dM/dH$ aligns with $H_c$ in systems featuring a solitary magnetic phase and a unimodal SFD, it is determined via the subsequent equation, serving as another crucial magnetic property [56].

$$SFD = \frac{\Delta H}{H_c} \tag{11}$$

In this context, $\Delta H$ represents the width at half the maximum peak of the, while $dM/dH$ is derived from differentiating the hysteresis loop. The SFD's values are tabulated in Table 3.

If the $SFD$ is smaller, the width at half the maximum peak of the $dM/dH$ curve will be smaller and the squareness of the hysteresis loop will be better [56]. This could be insured by the value of the $SR$ in Table 3. Among the samples, $BaFe_{11.5}Zn_{0.5}O_{19}$ exhibits the smallest SFD and the highest $SR$, indicating superior performance in this aspect. Consequently one can recommend this sample for recording media applications [2].

The increase in the $dM/dH$ peak indicates that the sample with a larger crystallite size and a well-crystallized structure has a magnetically stable state as shown in Fig. 12. $BaFe_{11.5}Zr_{0.5}O_{19}$ with the largest crystallite size exhibits the largest $dM/dH$ peak indicating the most stable magnetic state [56]. The presence of a single peak indicates a single magnetic phase. The second peak observed in BHF doped with $Ni$ and $Gd$ is due to the presence of impurities and secondary phases as detected in the XRD data.

### 3.3 Microwave high-frequency applications

Hexaferrites exhibit properties that make them highly effective in various applications. The high magnetic anisotropy, high resistivity, low eddy current losses at high frequencies, making the hexaferrite efficient in X-band applications [75]. There is an increasing need for hexaferrite materials for high-frequency applications, such as telecommunications and radar systems, as advancements in microwave technology require higher frequencies and bandwidths that can reach up to 100 GHz. BHF, which are nonconductive oxides, allow for the complete penetration of electromagnetic fields [75]. At these high frequencies, domain walls cannot follow the field variation resulting in microwave power absorption through spin dynamics. This dynamic behavior is conventionally described by the Landau-Lifshitz equation of motion, which can be represented in its undamped form by the following equation [75]

$$dM/dt = \gamma M \times Hi \tag{12}$$

where M denotes the magnetization, γ represents the gyromagnetic ratio (the ratio of mechanical to magnetic moment, defined as $\gamma = g\ \mu_B/\hbar$, with $\mu_B$ being the Bohr magneton and g referred to as the Landé splitting factor, which influences the rate at which energy levels split). The Landé g-factor is approximately $g = g_S \approx 2$, as indicated by the Landé equation, with $\gamma$ equating to 2.8 MHz/G [76].

Certain applications of doped BHF rely on the concept that the rotation of spins is affected by the alignment of an external H, which facilitates the modulation of interactions with microwave fields. When the H is aligned in a specific direction, the doped BHF permits the transmission of microwave frequency ($M$WF); however, when the field is reversed, it demonstrates significant absorption of those signals. This principle satisfies the operation of non-reciprocal devices, such as circulators and antennas [76, 77].

There has been an increasing interest in the phenomenon of nonresonant microwave power absorption at low H, commonly known as low-field microwave absorption

(LFA). This effect is notably affected by the anisotropy field of the ferrimagnetic materials. To evaluate the appropriateness of $BaFe_{11.5}D_{0.5}O_{19}$ for high-frequency microwave applications, we computed the MWF value, an essential parameter for devices that employ BHF, using the following equation [75]

$$\omega_m = 8\pi^2 M_s \gamma \tag{13}$$

where γ represents the gyromagnetic ratio (the ratio of mechanical to magnetic moment) as previously described. Doping with both magnetic and nonmagnetic cations into BHF results in a variation of the resonance frequency, in accordance with the principles of ferrimagnetic resonance theory. However, structural modifications from ion substitution ($Zr^{4+}$, $Gd^{3+}$, $Ni^{2+}$, $Zn^{2+}$) alter lattice parameters and cation distribution, which directly impact magnetic anisotropy and resonance frequencies. Additionally, the substitution-induced magnetic changes, such reduced coercivity or adjusted saturation magnetization, optimizes materials for high-frequency applications by minimizing energy losses and improving electromagnetic response. The microwave frequencies utilized for the samples are shown in Table 3.

The analysis indicates that all samples operate at frequencies between 8.5 and 13 GHz in the X band frequency range which is beneficial for the development of nano devices operating in super high frequency bands enabling the transmission and absorption of radio waves in electronic devices such as radar absorption and telecommunications. It has been observed that this range of microwave radiation affects microbial cultures. Consequently, it is strongly recommended to use the studied samples for applications in microwave super high frequency to effectively eliminate different bacteria [75].

## 4 Conclusion

The XRD analysis verifies that the samples prepared using the citrate auto-combustion method exhibit a perfect hexagonal structure, as indicated by the calculated *c/a* ratio. The isovalent substitution provides a lower crystallite size than the heterovalent substitution. Raman spectroscopy indicates a shift at the spin-down $4f_2$ site and a minor shift at the spin-down $4f_1$ site of $BaFe_{11.5}Gd_{0.5}O_{19}$, which accounts for its lowest magnetic saturation. The prepared samples exhibit high squareness ratio values, which are advantageous for permanent magnets. The highest saturation magnetization is achieved with $BaFe_{11.5}Zr_{0.5}O_{19}$, whereas $BaFe_{11.5}Zn_{0.5}O_{19}$ and $BaFe_{11.5}Gd_{0.5}O_{19}$ exhibit the greatest coercivity, rendering them suitable candidates for various magnetic recording applications. The analysis indicates that the prepared samples operate at frequencies between 8.5 and 13 GHz in the X band frequency range which is beneficial for the development of nano devices operating in super high frequency bands.

## Data availability

Data will be available upon request.

**Acknowledgements** I would like to express my gratitude and appreciation to Amira. T. Mohamed who worked actively in the final stage of revising the research.

**Author contributions** Y Yasser contributed to the preparation of the material, the gathering and analysis of data, formal analysis, inquiry, methodology, validity and visualization, reviewing, and editing. EE Ateia contributed with conceptualization, validation, data gathering and analysis, writing and preparing the original draft, supervision, visualization, reviewing, and editing. AS Shafaay contributed with material preparation, data curation, analysis, research, methodology, formal analysis, supervision, reviewing, and editing.

**Funding** Open access funding provided by The Science, Technology & Innovation Funding Authority (STDF) in cooperation with The Egyptian Knowledge Bank (EKB).

## Compliance with ethical standards

**Conflict of interest** The authors declare no competing interests.



## References

1. Mahapatro J, Agrawal S (2022) Optical, dielectric and electrical properties of $Gd^{3+}$ ions doped barium hexaferrite ceramic compounds for microwave device applications. J Alloy Compd 907:164405. https://doi.org/10.1016/j.jallcom.2022.164405
2. Ateia EE, Rabie O, Mohamed AT (2023) Multi-susceptible single-phased hexaferrite with significant magnetic switching properties by selectively doping. Phys Scr 98(6):065801. https://doi.org/10.1088/1402-4896/acd230
3. Hussein MS, Ateia EE, Nofal A, Morsy MA (2025) Impact of friction stir welding on the mechanical and microstructural

properties of austempered ductile iron and mild steel joints. J Alloy Metall Syst 9:100154
4. Tuyen NL, Hue NT, Tho PT, Toan HN, Xuan CTA, Dang NV, Ho TA, Tuan NQ, Tran N (2024) Excellent microwave absorption performance of zinc-doped $SrFe_{12}O_{19}$ hexaferrite and detailed loss mechanism. J Sci Adv Mater Devices 9(4):100796. https://doi.org/10.1016/j.jsamd.2024.100796
5. Pazhani N, Velavan R (2020) Microstructure and properties of barium hexaferrite nanoparticles. Malaya J Matematik S(2):4960–4965. https://doi.org/10.26637/MJM0S20/1279
6. Thi Kim Yen N, Quy Tuan N, Dat Trinh N, Truong Son Le V, Toan Dang N, Thi Le A, Tien Tran N, Tran N (2022) Detailed microwave absorption performance of $BaFe_{12}O_{19}$ nano-hexaplates with a large variety of thicknesses. Adv Nat Sci Nanosci Nanotechnol 13(2):025006. https://doi.org/10.1088/2043-6262/ac6c1f
7. Sheikh FA, Noor ul Huda Khan Asghar HM, Khalid M, Gilani ZA, Ali SM, Khan N-ul-H, Shar MA, Mufti H, Alhazaa A (2023) Dielectrically modified $Dy^{3+}$ substituted nickel-cobalt ferrites for high frequency devices. Phys B Condens Matter 652:414656. https://doi.org/10.1016/j.physb.2023.414656
8. Phalake SS, Somvanshi SB, Tofail SAM, Thorat ND, Khot VM (2023) Functionalized manganese iron oxide nanoparticles: a dual potential magneto-chemotherapeutic cargo in a 3D breast cancer model. Nanoscale 15(38):15686–15699. https://doi.org/10.1039/d3nr02816j
9. Joshi RS, Kumar PSA (2013) Magnetic Solid-State Materials. In: Comprehensive Inorganic Chemistry II, 2nd ed: From Elements to Applications, 4, Elsevier Ltd, 271–316. https://doi.org/10.1016/B978-0-08-097774-4.00413-7
10. Wang Y, Xiao R, Xiao N, Wang Z, Chen L, Wen Y, Li P (2022) Wireless Multiferroic Memristor with Coupled Giant Impedance and Artificial Synapse Application. Adv Electron Mater 8(10):2200370. https://doi.org/10.1002/aelm.202200370
11. Tho PT, Tran N, Tuan NQ, Ho TA, Xuan CTA, Toan HN, Lee BW (2023) Detailed microwave loss mechanisms for nanocomposites of *La*-doped $BaFe_{12}O_{19}$ and polyaniline. Ceram Int 49(14):23669–23679. https://doi.org/10.1016/j.ceramint.2023.04.201
12. Ahmed Sheikh F, Abbas Gilani Z, Noor ul Huda Khan Asghar HM, Khalid M, Mansoor Ali S, Khan N-ul-H, Ali Shar M, Khan AK (2023) Structural, morphological, and magneto-dielectric features of *Ni-Co-Pr* ferrites for high density memory and high frequency devices. J Magn Magn Mater 587:171240. https://doi.org/10.1016/j.jmmm.2023.171240
13. Tran N, Lee MY, Jeong WH, Phan TL, Tuan NQ, Lee BW (2021) Thickness independent microwave absorption performance of *La*-doped $BaFe_{12}O_{19}$ and polyaniline composites. J Magn Magn Mater, 538, https://doi.org/10.1016/j.jmmm.2021.168299
14. Verma S, Chawla A, Pushkarna I, Singh A, Kumar Godara S, Kumar Pathak D, Kumar R, Singh M (2021) Understanding the phase evolution with temperature in pure ($BaFe_{12}O_{19}$) and zinc-zirconium co-doped barium hexaferrite ($BaZnZrFe_{10}O_{19}$) samples using Pawley and Rietveld analysis. Mater Today Commun 27:102291. https://doi.org/10.1016/j.mtcomm.2021.102291
15. Bhosale AB, Somvanshi SB, Murumkar VD, Jadhav KM (2020) Influential incorporation of RE metal ion ($Dy^{3+}$) in yttrium iron garnet (*YIG*) nanoparticles: Magnetic, electrical and dielectric behaviour. Ceram Int 46(no. 10):15372–15378. https://doi.org/10.1016/j.ceramint.2020.03.081
16. Kumar N, Shukla A, Choudhary RNP (2021) Studies of structural, electrical and multiferroic features of Fe-site co-substituted (*Ni, Ti*) bismuth ferrite: $Bi(Ni_{0.35}Ti_{0.35}Fe_{0.30})O_3$. Springer Science and Business Media Deutschland GmbH. https://doi.org/10.1007/s00339-021-04853-7
17. Kharat PB, Somvanshi SB, Dawi EA, Mopari AM, Bansod NH (2024) Exploring the electrochemical performance of nickel-zinc ferrite nanoparticles for supercapacitor applications. J Mater Sci Mater Electronics, 35(8), https://doi.org/10.1007/s10854-024-12360-7
18. Singh VP, Jasrotia R, Kumar R, Raizada P, Thakur S, Batoo KM, Singh M (2018) A Current Review on the Synthesis and Magnetic Properties of M-Type Hexaferrites Material. World J Condens Matter Phys 08(2):36–61. https://doi.org/10.4236/wjcmp.2018.82004
19. Maswadeh Y, Mahmood SH, Awadallah A, Aloqaily AN (2015) Synthesis and structural characterization of nonstoichiometric barium hexaferrite materials with Fe:Ba ratio of 11.5-16.16. In IOP Conference Series: Materials Science and Engineering, Institute of Physics Publishing, https://doi.org/10.1088/1757-899X/92/1/012019
20. Manglam MK, Kumari S, Mallick J, Kar M (2021) Crystal structure and magnetic properties study on barium hexaferrite of different average crystallite size. Appl Phys A Mater Sci Process 127(2), https://doi.org/10.1007/s00339-020-04232-8
21. Sharma S, Satyapal HK, Kumar SS, Aryan R, Manash A, Kumar V (2021) Effect of $Gd^{3+}$ substitution on the structural and magnetic properties of barium hexaferrite nanomaterials. Mater Today Proc, 2587–2592. https://doi.org/10.1016/j.matpr.2020.12.650
22. Himanshi, Jasrotia R, Prakash J, Verma R, Thakur P, Kandwal A, Wan F, Thakur A (2023) Synthesis, characterization, and applications of doped barium hexaferrites: A review. Phys B Condens Matter 667:415202. https://doi.org/10.1016/j.physb.2023.415202
23. Lee H, Ryu SH, Kwon SJ, Choi JR, Lee Sbok, Park B (2023) Absorption-Dominant mmWave EMI Shielding Films with Ultralow Reflection using Ferromagnetic Resonance Frequency Tunable M-Type Ferrites. Nanomicro Lett 15(1):76. https://doi.org/10.1007/s40820-023-01058-w
24. Tanwar K, Gyan DS, Gupta P, Pandey S, Omparkash, Kumar D (2018) Investigation of crystal structure, microstructure and low temperature magnetic behavior of $Ce^{4+}$ and $Zn^{2+}$ co-doped barium hexaferrites (BaFe12O19). RSC Adv 8(35):19600–19609. https://doi.org/10.1039/c8ra02455c
25. Peng H, Yang P, Yang P, Qi H (2023) Design, fabrication, and magnetic properties of novel (*Ni,Cr,Zr*)-co-doped M-type barium ferrite ceramics. Ceram Int 49(13):21577–21586. https://doi.org/10.1016/j.ceramint.2023.03.294
26. Xu Z, Liu H, Zhou W, Yu W, Xiao G, Lu D, Gao F, Cheng Z, Luo G (2024) Effect of Gd doping on the structural, magnetic and dielectric properties of Y-type hexaferrite $BaSrCo_2(Fe_{1-x}Gd_x)_{11}AlO_{22}$ ceramics. Ceram Int 51:2947–2955. https://doi.org/10.1016/j.ceramint.2024.11.271
27. Yamaoka H, Jarrige I, Tsujii N, Lin JF, Ikeno T, Isikawa Y, Nishimura K, Higashinaka R, Sato H, Hiraoka N, Ishii H, Tsuei KD (2011) Strong coupling between 4f valence instability and 3d ferromagnetism in $Yb_xFe_4Sb_{12}$ studied by resonant x-ray emission spectroscopy. Phys Rev Lett 107(17):177203. https://doi.org/10.1103/PhysRevLett.107.177203
28. Jadhav SA, Somvanshi SB, Gawali SS, Zakde K, Jadhav KM (2024) Rare earth-doped mixed *Ni–Cu–Zn* ferrites as an effective photocatalytic agent for active degradation of Rhodamine B dye. J Rare Earths 42(3):488–496. https://doi.org/10.1016/j.jre.2023.03.004
29. Mahadevan S, Sankar AR, Singh S, Sharma P (2023) Enhanced X-band absorption and shielding performance of *Gd*-substituted barium hexaferrite, J Alloys Compd, 959, https://doi.org/10.1016/j.jallcom.2023.170456
30. Somvanshi SB, Jadhav SA, Khedkar MV, Kharat PB, More SD, Jadhav KM (2020) Structural, thermal, spectral, optical and surface analysis of rare earth metal ion ($Gd^{3+}$) doped mixed *Zn–Mg* nano-spinel ferrites. Ceram Int 46(9):13170–13179. https://doi.org/10.1016/j.ceramint.2020.02.091
31. Khan NulH, Abbas Gilani Z, Khalid M, Noor ul Huda Khan Asghar HM, Hussain G, Ali Shar M, Mansoor Ali S, Azhar Khan M, Ahmed Sheikh F, Alhazaa A (2023) Impact of cerium

substitution cobalt–zinc spinel ferrites for the applications of high frequency devices. Phys B Condens Matter 660:414873. https://doi.org/10.1016/j.physb.2023.414873
32. Humbe AV, Kounsalye JS, Somvanshi SB, Kumar A, Jadhav KM (2020) Cation distribution, magnetic and hyperfine interaction studies of *Ni-Zn* spinel ferrites: Role of Jahn Teller ion (Cu2+) substitution. Mater Adv 1(4):880–890. https://doi.org/10.1039/d0ma00251h
33. Ateia EE, Abdelamksoud MK, Arman MM, Ramadan R, Shafaay AS (2019) Optimizing the physical properties of cobalt/graphene nanocomposites for technological applications. Appl Phys A Mater Sci Process, 125(8), https://doi.org/10.1007/s00339-019-2815-2
34. Ateia EE, Ramadan R, Shafaay AS (2020) Efficient treatment of lead-containing wastewater by $CoFe_2O_4$/graphene nanocomposites. Appl Phys A Mater Sci Process, 126(3), https://doi.org/10.1007/s00339-020-3401-3
35. Ateia EE, Rabie O, Mohamed AT (2024) Magneto-fluorescent core–shell $Sr_{0.8}La_{0.2}Fe_{11}CuO_{19}$ @ CQDs for the detection of metal ions. Appl Surf Sci, 678, https://doi.org/10.1016/j.apsusc.2024.161123
36. Xuan CTA, Toan HN, Ha PTV, Ho TA, Thanh TD, Tuan NQ, Tho PT, Tran N (2024) Microwave absorption performance for *Cu, Co*, and *Ti* co-doped $SrFe_{12}O_{19}$ as a function of incident angle. Mater Chem Phys 317:129174. https://doi.org/10.1016/j.matchemphys.2024.129174
37. Gulbadan S, Ejaz SR, Nizamani AH, Shakir I, Agboola PO, Akhtar MN, Warsi MF, Khan MA (2020) Structural elucidation and dielectric behavior evaluation of sol-gel synthesized *Co–Al* co-substituted M-type hexaferrite materials. Ceram Int 46(no. 4):4914–4923. https://doi.org/10.1016/j.ceramint.2019.10.228
38. Topkaya R (2017) Effect of Zn substitution on temperature dependent magnetic properties of $BaFe_{12}O_{19}$ hexaferrites. J Alloy Compd 725:1230–1237. https://doi.org/10.1016/j.jallcom.2017.07.248
39. Somvanshi SB, Khedkar MV, Kharat PB, Jadhav KM (2020) Influential diamagnetic magnesium ($Mg^{2+}$) ion substitution in nano-spinel zinc ferrite ($ZnFe_2O_4$): Thermal, structural, spectral, optical and physisorption analysis. Ceram Int 46(no. 7):8640–8650. https://doi.org/10.1016/j.ceramint.2019.12.097
40. Raut VK, Somvanshi SB, Dawi EA, Birajdar CT (2024) Facile sol–gel synthesis of trivalent $Al^{3+}$-$Gd^{3+}$ ions co-doped nanoscale cobalt spinel ferrite for magneto-electronic applications. Inorg Chem Commun 168:112907. https://doi.org/10.1016/j.inoche.2024.112907
41. Raut VK, Somvanshi SB, Dawi EA, Birajdar CT (2024) Sol-gel auto combustion synthesis of $Al^{3+}$-$Gd^{3+}$ ions co-doped cobalt ferrite nanoparticles for nanoelectronics applications. J Solgel Sci Technol, https://doi.org/10.1007/s10971-024-06571-x
42. Wartewig P, Krause MK, Esquinazi P, Rosler S, Sonntag R(1999) Magnetic properties of Zn- and Ti-substituted bariumhexaferrite. J Magn Magn Mater 192:83–99
43. Jadhav SA, Khedkar MV, Somvanshi SB, Jadhav KM (2021) Magnetically retrievable nanoscale nickel ferrites: An active photocatalyst for toxic dye removal applications. Ceram Int 47(20):28623–28633. https://doi.org/10.1016/j.ceramint.2021.07.021
44. Poedji H, Fahma R, Siska S (2015) Synthesis of CuFe O4-Bentonite Composite for Adsorption of Ni(II) from Electroplating Wastewater. Adv Mat Res 1112:213–216, Trans Tech Publications, Switzerland, https://doi.org/10.4028/www.scientific.net/AMR.1112.213
45. Ateia EE, Gawad D, Arman MM (2024) Core-shell nanomaterials based on $La_2FeCrO_6$ coated with metal oxides for optical applications. Phys Scr, 99(11), https://doi.org/10.1088/1402-4896/ad80e6
46. Mostafa MYA, Mostafa A, Abdel-Rahman M, Assem EE, Ashour A, Badawi EA (2023) XRD peak broadening modelling for Al-alloys characterization compared with Rietveld profile analysis. Mater Today Proc, https://doi.org/10.1016/j.matpr.2023.04.252
47. Bhosale RR, Barkule RS, Shengule DR, Jadhav KM (2013) Synthesis, structural, electrical and dielectric properties of *Zn-Zr* doped strontium hexaferrite nanoparticles. J Mater Sci Mater Electron 24(no. 8):3101–3107. https://doi.org/10.1007/s10854-013-1217-z
48. Rajenimbalkar RS, Ghuge SS, Deshmukh VJ, Dawi EA, Somvanshi SB (2024) Effect of $Zn^{2+}$–$Ti^{4+}$ co-doping on the structural, infrared, surface, magnetic, electric and dielectric parameters of nanoscale $CoFe_2O_4$, J Mater Sci Mater Electronics, 35(27), https://doi.org/10.1007/s10854-024-13567-4
49. Long X, Chong K, Su Y, Du L, Zhang G (2023) Connecting the macroscopic and mesoscopic properties of sintered silver nanoparticles by crystal plasticity finite element method. Eng Fract Mech, 281, https://doi.org/10.1016/j.engfracmech.2023.109137
50. Danish M, Islam M, Ahmad F, Madni MN, Jahangeer M (2024) Synthesis of M-type hexaferrite reinforced graphene oxide composites for electromagnetic interference shielding. J Phys Chem Solids, 185, https://doi.org/10.1016/j.jpcs.2023.111783
51. Muhiuddin G, Bibi I, Nazeer Z, Majid F, Kamal S, Kausar A, Raza Q, Alwadai N, Ezzine S, Iqbal M (2023) Synthesis of Ni doped barium hexaferrite by microemulsion route to enhance the visible light-driven photocatalytic degradation of crystal violet dye. Ceram Int 49(3):4342–4355. https://doi.org/10.1016/j.ceramint.2022.09.319
52. Kim CS, Yoon S (2023) Magnetic characterization of $La^{3+}$ and $Li^{1+}$ co-substituted M-type strontium hexaferrite. AIP Adv, 13(2), https://doi.org/10.1063/9.0000491
53. Wei Y, Sun X, Meng X, Li Z, Zhang L, Zhou K, Ma Z (2024) Enhancing the properties of Cd-free *MgZnS* buffer for solar cells by co-sputtering *ZnS* and Mg targets. Mater Today Commun 39:108766. https://doi.org/10.1016/j.mtcomm.2024.108766
54. Mehnert KI, Häßner M, Dreer YM, Biswas I, Niewa R (2023) Crystal Structure and XPS Study of Titanium-Substituted M-Type Hexaferrite $BaFe_{12-x}Ti_xO_{19}$, Inorganics, 11(5), https://doi.org/10.3390/inorganics11050207.
55. Renuka L, Anantharaju KS, Vidya YS, Nagaswarupa HP, Prashantha SC, Sharma SC, Nagabhushana H, Darshan GP (2017) A simple combustion method for the synthesis of multi-functional $ZrO_2$/*CuO* nanocomposites: Excellent performance as Sunlight photocatalysts and enhanced latent fingerprint detection. Appl Catal B 210:97–115. https://doi.org/10.1016/j.apcatb.2017.03.055
56. Pan X, Sun A, Han Y, Zhang W, Zhao X (2018) Effects of different sintering temperature on structural and magnetic properties of *Ni-Cu-Co* ferrite nanoparticles. Modern Phys Lett B, 32, https://doi.org/10.1142/S0217984918503219
57. Pesin LA, Gudkova SA, Zhivulin VE, Pavlova KP, Starikov AY, Sherstyuk DP, Lebedev AM, Chumakov RG, Vinnik DA (2023) Effect of Titanium and Manganese Additions on the Surface Segregation of Barium in Hexaferrites. J Struct Chem 64(12):2358–2369. https://doi.org/10.1134/S0022476623120077
58. Ateia EE, Elsayed K, El-Nashar DE (2023) Tuning the properties of $NBR/BaFe_{11.5}Co_{0.5}O_{19}$: a road toward diverse applications. Appl Phys A Mater Sci Process, 129(2), https://doi.org/10.1007/s00339-023-06388-5.
59. Jing XD, Li ZG, Chen ZT, Li ZY, Qin CY, Gong HY (2023) Effect of praseodymium valence change on the structure, magnetic, and microwave absorbing properties of M-type strontium ferrite: the mechanism of influence of citric acid dosage and calcination temperature. Mater Today Chem, 30, https://doi.org/10.1016/j.mtchem.2023.101537.
60. Khongorzul B, Jargalan N, Tsogbadrakh N, Odkhuu D, Trukhanov SV, Trukhanov AV, Sangaa D (2023) Correlation of the crystal features, magnetic parameters, and electronic structure of *Bi*-substituted $BaFe_{12-x}Bi_xO_{19}$ hexaferrites: Theoretical background. Ceram Int 49(10):15492–15499. https://doi.org/10.1016/j.ceramint.2023.01.134

61. Ateia EE, Ateia MA, Arman MM (2022) Assessing of channel structure and magnetic properties on heavy metal ions removal from water. J Mater Sci Mater Electron 33(11):8958–8969. https://doi.org/10.1007/s10854-021-07008-9
62. Wang S, Gao H, Sun G, Zhang J, Xia Y, Xie C, Yang G, Wang Y, Fang L (2021) M-type Barium Hexaferrite Nanoparticles Synthesized by γ-Ray Irradiation Assisted Polyacrylamide Gel Method and Its Optical, Magnetic and Supercapacitive Performances. J Clust Sci 32(3):569–578. https://doi.org/10.1007/s10876-020-01815-6
63. Sehar F, Anjum S, Mansoor A, Mustafa Z (2021) Formation of non-centrosymmetric covalent bonds due to the substitution of cobalt contents in M-type barium hexa-ferrites $BaFe_{(12-x)}O_{19}$. Appl Phys A Mater Sci Process, 127, https://doi.org/10.1007/s00339-021-04762-9
64. Mahmood SH, Mahmood SH, Dushaq GH, Bsoul I, Awawdeh M, Juwhari HK, Lahlouh BI, AlDamen MA (2014) Magnetic Properties and Hyperfine Interactions in M-Type $BaFe_{12-2x}Mo_xZn_xO_{19}$ Hexaferrites. J Appl Math Phys 02(05):77–87. https://doi.org/10.4236/jamp.2014.25011
65. Chauhan CC, Kagdi AR, Jotania RB, Upadhyay A, Singh Sandhu C, Shirsath SE, Singh Meena S (2018) Structural, magnetic and dielectric properties of *Co-Zr* substituted M-type calcium hexagonal ferrite nanoparticles in the presence of $\alpha$-$Fe_2O_3$ phase. Ceram Int 44(15):17812–17823. https://doi.org/10.1016/j.ceramint.2018.06.249
66. Kanagesan S, Jesurani S, Velmurugan R, Kalaivani T (2012) Preparation and magnetic properties of *Ni-Zr* doped barium strontium hexaferrite. J Mater Sci Mater Electron 23(4):952–955. https://doi.org/10.1007/s10854-011-0526-3
67. Sharrouf M, Awad R, Habanjar K (2023) Investigation of the structural, morphological and magnetic properties of barium hexaferrite added with magnesium oxide nanoparticles. Appl Phys A Mater Sci Process, 129, https://doi.org/10.1007/s00339-023-07079-x
68. Bharati VA, Somvanshi SB, Humbe AV, Murumkar VD, Sondur VV, Jadhav KM (2020) Influence of trivalent *Al–Cr* co-substitution on the structural, morphological and Mössbauer properties of nickel ferrite nanoparticles. J Alloy Compd 821:153501. https://doi.org/10.1016/j.jallcom.2019.153501
69. Lestari A, Kasim K, Utami M, Deksino GR (2023) Microwave Absorbing Improvement of Barium M-Hexaferrite by *Ni* Doping. Int J Soc Sci Res Rev, https://doi.org/10.47814/ijssrr.v6i1.765
70. Hu J, Liu C, Kan X, Liu X, Feng S, Lv Q, Yang Y, Wang W, Shezad M, Mehmood Ur Rehman K (2020) Structure and magnetic performance of *Gd* substituted Sr-based hexaferrites. J Alloy Compd 820:153180. https://doi.org/10.1016/j.jallcom.2019.153180
71. Asif SU, Solre GFB, Abdu Musad Saleh E, Saeedi AM, Moharam MM, Malik AR, Ibrahim FA, Hamdy MS, Hassan AM, Bashir R, Ijaz M (2024) Structural and Magnetic Impressions of Rare Earth *Tb* Doping on *Ba–In* Based Hexaferrites Prepared Through Sol–Gel Route for Magnetic Aspects. J Inorg Organomet Polym Mater 34(no. 6):2510–2521. https://doi.org/10.1007/s10904-023-02989-y
72. Sheikh FA, Noor ul Huda Khan Asghar HM, Khalid M, Gilani ZA, Ali SM, Khan N-ul-H, Shar MA, Alhazaa A (2023) Synthesis of $Ce^{3+}$ substituted *Ni-Co* ferrites for high frequency and memory storage devices by sol-gel route. J Alloy Compd 938:168637. https://doi.org/10.1016/j.jallcom.2022.168637
73. Naeem Ashiq M, Sami Asi A, Farooq S, Najam-ul-Haq M, Rehman S (2017) Magnetic and electrical properties of M-type nano-strontium hexaferrite prepared by sol-gel combustion method. J Magn Magn Mater 444:426–431. https://doi.org/10.1016/j.jmmm.2017.08.065
74. Pullar RC (2012) Hexagonal ferrites: A review of the synthesis, properties and applications of hexaferrite ceramics, 2012. https://doi.org/10.1016/j.pmatsci.2012.04.001
75. Dhage VN, Mane ML, Keche AP, Birajdar CT, Jadhav KM (2011) Structural and magnetic behaviour of aluminium doped barium hexaferrite nanoparticles synthesized by solution combustion technique. Phys B Condens Matter 406(4):789–793. https://doi.org/10.1016/j.physb.2010.11.094
76. Ateia EE, Meleka KK, Singh C, Ghobrial FZ, El-Bassuony A, Ghafar DN (2024) The synthesis of $CoAl_{0.3}Fe_{1.7}O_4/SmFeO_3$ nanocomposites with enhanced properties for technological applications. J Mater Res 39(7):1168–1180. https://doi.org/10.1557/s43578-024-01301-z
77. Shao N, Li J, Che S, Zheng J, Qiao L, Ying Y, Yu J, Li W (2024) Effect of magnetization on magnetic and dielectric properties of *Z/BaM* hexaferrite composite materials. J Magn Magn Mater 594:171476. https://doi.org/10.1016/j.jmmm.2023.171476
78. Ateia EE, Saeid YA, Abdelmaksoud MK (2023) Synthesis and Characterization of $CaFe_{1.925}Gd_{0.025}Sm_{0.05}O_4$/PEG Core–Shell Nanoparticles for Diverse Applications. J Supercond Nov Magn 36(no. 3):1011–1024. https://doi.org/10.1007/s10948-023-06535-2